RSC Advances

PAPER

View Article Online
View Journal | View Issue

Check for updates

Cite this: *RSC Adv.*, 2025, **15**, 19546

Influence of phosphorus activation and carbonization temperature on the electrochemical performance of hard carbon made from olive pomace as an anode for sodium-ion batteries†

Imad Alouiz,[a] Mohamed Aqil,[b] Abdelwahed Chari,[b] Mouad Dahbi,[b] Mohamed Yassine Amarouch[a] and Driss Mazouzi *[a]

Carbon electrode materials derived from biomass have attracted important interest in studying high-performance electrochemical energy storage devices that are environmentally friendly. Therefore, this study focuses on producing hard carbon (HC) from olive pomace. This is evaluated as a negative electrode in a sodium-ion battery (SIB) with a primary purpose of evaluating the effect of carbonization temperature on HC properties. The preparation of HC from olive pomace was carried out using a chemical activation method with phosphoric acid as an activator and then carbonizing at different temperatures. The generated solid carbon was characterized using various analytical methods, including SEM, HR-TEM, Raman spectroscopy, XRD, FTIR, TGA, and BET. The findings demonstrated that the carbonization temperature significantly affected the morphology, structural characteristics, and disorder level of the synthesized carbon materials. The resultant materials exhibit initial discharge/charge specific capacities for sodium-ion batteries of 307/146, 408/193, and 404/272 mA h g^{-1} for HC-750, HC-1000, and HC-1250 °C electrodes, respectively, giving an initial coulombic efficiency ratio of 47%, 48%, and 67%. The electrochemical evaluations indicated that HC carbonized at elevated temperatures, particularly at 1250 °C, exhibited superior performance characteristics. Following 100 cycles, a capacity of 248 mA h g^{-1} was achieved, accompanied by an exceptional capacity retention ratio of 99.9% and good rate capabilities. These results illuminate the significance of the chemical activation process (phosphorus doping) and the carbonization temperature in enhancing electrode performance. By employing this methodology, the utilization of olive pomace effectively yields sustainable biomass-derived HCs in the fabrication of cost-efficient negative materials with enhanced performance for sodium-ion batteries.

Received 11th April 2025
Accepted 10th May 2025

DOI: 10.1039/d5ra02547h

rsc.li/rsc-advances

Open Access Article. Published on 10 June 2025. Downloaded on 1/23/2026 5:39:04 AM.
This article is licensed under a Creative Commons Attribution-NonCommercial 3.0 Unported Licence.

1. Introduction

The growing demand for electronic devices, electric vehicles, and large-scale, energy storage systems worldwide has caused major challenges in developing long-term and effective energy storage solutions.[1] In this regard, rechargeable batteries are of utmost significance, in particular, lithium-ion (LIB) and sodium-ion (SIB) batteries.[2,3] Although LiBs are currently a leader for their high energy density and excellent long cycle life. Concerns about rising costs and the limited availability of lithium resources have led to the search for viable alternatives, such as SIBs.[4,5] Indeed, SIBs offer many attractive features and notable benefits.

Given that sodium is one of the most abundant elements on Earth, this could potentially significantly reduce battery costs.[6,7] Furthermore, the possibility of using an aluminum current collector that is cheaper and lighter than copper is a key advantage of this type of technology.[8] In fact, research on sodium-ion batteries first began in the 1970s. However, progress is not being accelerated due to the relative ease of handling of sodium-based materials, which are more sensitive to moisture than their lithium counterparts, as well as the competitive energy density of SIBs.[9] Nevertheless, in recent years, the rising cost of lithium, cobalt, and nickel, associated with concerns over limited lithium reserves, has reignited interest in SIBs as a potential alternative, prompting the redevelopment of this previously technology.[10,11]

In order to commercialize SIBs, it is essential to develop highly efficient electrode materials. Thus, the most important

[a]*R.N.E Laboratory, Multidisciplinary Faculty of Taza, University Sidi Mohamed Ben Abdellah, Fez, Morocco. E-mail: driss.mazouzi@usmba.ac.ma*

[b]*MSN Materials Science, Energy, and Nano-engineering Department, Mohammed VI Polytechnic University, Ben Guerir, Morocco*

† Electronic supplementary information (ESI) available. See DOI: https://doi.org/10.1039/d5ra02547h

© 2025 The Author(s). Published by the Royal Society of Chemistry

Open Access Article. Published on 10 June 2025. Downloaded on 1/23/2026 5:39:04 AM. This article is licensed under a Creative Commons Attribution-NonCommercial 3.0 Unported Licence.

components of SIBs, such as cathodes, anodes, and electrolytes, have been the subject of numerous studies in this field. However, the development of stable negative electrode materials for SIBs remains a major challenge.[12] Indeed, negative electrode materials must meet essential requirements, such as high reversible load capacity, good efficiency and long cycle.[10] Graphite is the most frequently used anode in LIBs due to its abundance, affordability, and non-toxic properties. Nevertheless, the insertion of sodium ions into graphite is difficult due to the small distance between the graphite layers, which cannot easily accommodate the large sodium ions, whose radius is around 36% larger than that of lithium ions.[10,13] Therefore, using graphite as the anode of the SIB is not practical. To address this limitation, the focus is on intensive research on alternative materials divided into three major categories according to the reaction mechanism in the process of charging and discharge, namely the insertion of reactions, conversion reactions, and alloy reactions.[14] Among these, carbonaceous materials and titanium-based oxides have been investigated for their insertion capabilities.[15–17] Furthermore, the conversion reaction examines anode materials such as transition metal oxides and sulfides.[14] However, Na-metal alloys are considered promising candidates, especially when combined with a conductive carbon matrix, which enhances their specific capacity and cycling stability. However, materials based on the reaction of alloys and conversions encounter serious disadvantages due to the large volume expansion during the process of insertion/de-insertion of the host material, causing continuous degradation of the electrode structure.[18,19] Among these options, hard carbon (HC) is highlighted as a promising candidate for SIB anodes, providing high specific capacity and stability. Despite this, it remains a challenge due to low initial coulombic efficiency (ICE) and limited electrical conductivity.[20,21]

Recently, several studies have focused on the elaboration of HC from abundant biomass such as peanut shells,[22] orange peels,[23] sugarcane bagasse,[24] tea waste,[25] argan shells,[26] and date palm pulp.[27] These precursors' abundance, low prices, environmental friendliness, and limitless architectural potential make them excellent choices for the synthesis of anode materials for SIBs.[28] There are many approaches to improving the electrochemical performance of these hard carbons, including synthesis conditions, porous structure created by an activating agent, and doping technology.[29–31] Studies have reported that HC material prepared at high temperatures exhibit high specific capacity, highlighting the correlation between the importance of closed pore volume and its sodium storage capacity.[26,27,32] By doping HCs with heteroatoms and introducing functional groups such as oxygen, it can be made to optimize their surface chemistry and enhance the capacity and stability of the solid-electrolyte interface (SEI).[31] The HC derived from biomass has high porosity and a controllable pore size distribution. This is important in facilitating sodium ion intercalation and improving cyclic battery performance. These properties make HC obtained particularly suitable for applications in sodium-ion batteries, offering both durability and efficiency.

Olive pomace (OP) is waste product that is usually discarded as part of the olive oil extraction process. This poses several environmental problems. In effect, these residues are generated in large quantities by the olive oil industry, posing waste management problems.[33,34] Among the promising approaches to recovering its by-product is the conversion of this waste into hard carbon that can be used in sodium-ion batteries.

This article focuses on studying a simple and efficient synthesis process to prepare hard carbon from olive pomace. For this, after chemical activation of olive pomace raw (OP-R) with phosphoric acid solution, the activated olive pomace (OP-A) is carbonized under an argon atmosphere at three temperatures ranging from 750 °C, 1000 °C and 1250 °C. In order to evaluate the influence of the chemical activation, OP-R was also carbonized directly at 1250 °C without chemical activation step to understand the importance of this step on HC performance. The structural and morphological properties of the produced HC were characterized using different spectroscopic techniques, including thermogravimetric (TG), Fourier transform infrared spectroscopy (FT-IR), scanning electron microscopy (SEM), transmission electron microscopy (HR-TEM), X-ray diffraction (XRD), Raman spectroscopy, and BET surface area measurement. To investigate the electrochemical properties of HCs samples used as anode materials for SIB applications, galvanostatic cycle tests (GCPL), cyclic voltammetry (CV), galvanostatic intermittent titration (GITT), and electrochemical impedance spectroscopy (EIS) were used. Olive pomace's hard carbon has a good specific capacity and cyclic stability, according to electrochemical experiments. This is particularly suitable for applications involving SIBs. Therefore, by valorizing olive pomace for the production of hard carbon, this approach addresses the problems associated with waste management and aids in the advancement of sustainable and effective energy storage solutions.

2. Materials and methods

2.1. Preparing hard carbon from olive pomace

Activation and carbonization are the two main processes used in this work, preparing hard carbon from OP-R. First, OP-R was impregnated in a phosphoric acid solution (H_3PO_4, 22% vol) at 50 °C for 2 hours to chemically activate olive pomace. The OP-A was then neutralized with sodium hydroxide (NaOH, 0.1 mol L^{-1}) to remove excess acid.[35] Then, OP-A is heated in a tube furnace that can be programmed under an argon atmosphere. The temperature was gradually increased at a rate of 5 °C min^{-1} from ambient temperature to the set temperature. Three carbonization temperatures were selected: 750 °C (HC-750 °C), 1000 °C (HC-1000 °C), and 1250 °C (HC-1250 °C). Each sample was kept at the selected temperature for 1 hour, resulting in different carbonization conditions. Furthermore, a sample of olive pomace was carbonized directly without a chemical activation step (OP-1250 °C) was prepared to understand the importance of this step on the properties and electrochemical performance of HC as anodes for SIBs (Fig. S1†).

Open Access Article. Published on 10 June 2025. Downloaded on 1/23/2026 5:39:04 AM. This article is licensed under a Creative Commons Attribution-NonCommercial 3.0 Unported Licence.

2.2. Material characteristics

The microcrystalline structure and structural properties of the carbonaceous materials were characterized by using a Bruker D8 Advance X-ray diffractometer (XRD; Cu Kα radiation (40 kV, $\lambda = 0.15418$ nm) at a scanning speed of 3° min^{-1} between 10° and 80°), and, Fourier transform infrared spectroscopy (FT-IR; PerkinElmer 1720 FT-IR spectrometer in the 600–4000 cm^{-1} wavenumber range). Graphitization degree of the HC was analyzed by Raman scattering spectroscopy (HORIBA LabRAM-HR Evolution) under green laser excitation ($\lambda = 532$ nm) in line-of-sight mode. The morphology of the samples was observed *via* scanning electron microscopy (SEM, Zeiss EVO MA10), and, high-resolution transmission electron microscopy (HR-TEM, Talos F200S, FEI, Thermo, Czech Republic) equipped with an energy-dispersive X-ray spectroscopy detector. Thermal decomposition data for olive pomace biomass was studied by thermogravimetric analysis using a Mettler Toledo TGA at a heating rate of 10 °C min^{-1} from 30 to 700 °C, under an oxygen atmosphere. The specific surface area and pore sizes were tested by N_2 adsorption–desorption using a Micromeritics ASAP 22460 analyzer.

2.3. Electrochemical measurements

Coin cells were used to evaluate the electrochemical performance of each sample as an anode material. A mixture of 80 wt% active material, 15 wt% carbon black, and 5 wt% polyvinylidene fluoride (PVDF) binder was combined to prepare the negative electrodes. The PVDF binder was dissolved in *N*-methyl-2-pyrrolidone (NMP) solvent, and the mixture was stirred until a homogeneous paste formed. This suspension was then coated onto aluminum foil. After coating, the film was dried at 70 °C for 1 hour to ensure proper adhesion and stability. The 12 mm diameter electrodes were dried overnight at 120 °C in a vacuum oven. The mass loading of these electrodes was 1.6–2.5 mg cm^{-2}. Then, the half-cells were built under an argon atmosphere in a glove box, in a two-electrode system with pure sodium metal as a counter and reference electrode. A glass fiber (Whatman) was used as a separator. The electrolyte used was sodium hexafluorophosphate ($NaPF_6$, 1 mol L^{-1}) in a mixture of ethylene carbonate (EC) and diethylene carbonate (DEC) (1 : 1 by volume). The performance of galvanostatic cycling with potential limitation (GCPL) was tested between 0.01 and 2.5 V at room temperature at a current density of 25 mA g^{-1} using a BCS-BioLogic battery cycler. Cyclic voltammetry (CV) measurements were performed on an electrochemical workstation using a BCS-800 potentiostat within a voltage window of 0.01–3 V *vs.* Na/Na^+ at scan rates of 0.1, 0.2, 0.5, 0.8, and 1.2 mV s^{-1}. Electrochemical impedance spectroscopy (EIS) measurements were performed in a frequency range of 100 kHz to 10 mHz.

3. Results and discussion

3.1. Structure and characterization

To identify and understand the molecular structure properties of the raw material, the Fig. 1A presents the FTIR spectrum of the OP-R. The spectrum mainly shows the presence of two vibrational peaks at 3600–3250 cm^{-1} and 2920 cm^{-1} corresponding to the stretches of –OH and C–H group, highlighting the presence of characteristic functional groups in lignocellulosic biomass.[36,37] Additionally, the band is located in the region 950–1130 cm^{-1} that characterizes the C–O group present in acids, alcohols, ethers, and esters.[37] However, the total disappearance of O–H peaks in the structure of the hard carbon produced, combined with the reduction in intensity of the other peaks observed during carbonization (Fig. 1B), demonstrates the progressive decomposition of cellulose. This phenomenon favors the formation of carbon structures.[38] In particular, the decrease in intensity of the peak at 1630 cm^{-1} is due to the C=O stretching vibration of carbonyl groups,[39] indicating a reduction in carbonyl functional groups after carbonization (Fig. S3†). On the other hand, the increase in peak intensity at 1700 cm^{-1} in HC, attributed to C=C at the aromatic ring,[40] shows a significant shift in molecular structure towards more conjugated and aromatic arrangements. We also observed that the peak at

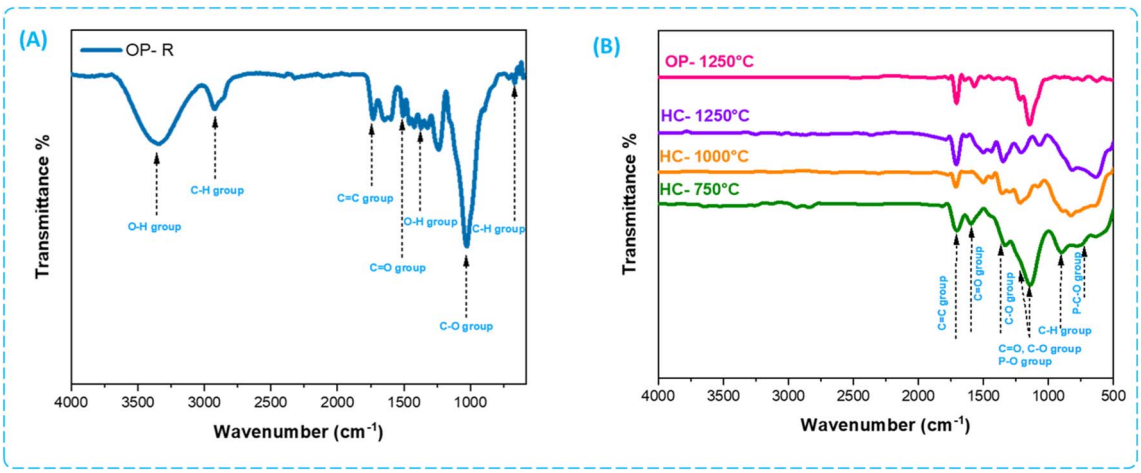

Fig. 1 (A) FT-IR spectra of OP-R, (B) of HCs obtained for different temperatures.

© 2025 The Author(s). Published by the Royal Society of Chemistry

Open Access Article. Published on 10 June 2025. Downloaded on 1/23/2026 5:39:04 AM.
This article is licensed under a Creative Commons Attribution-NonCommercial 3.0 Unported Licence.

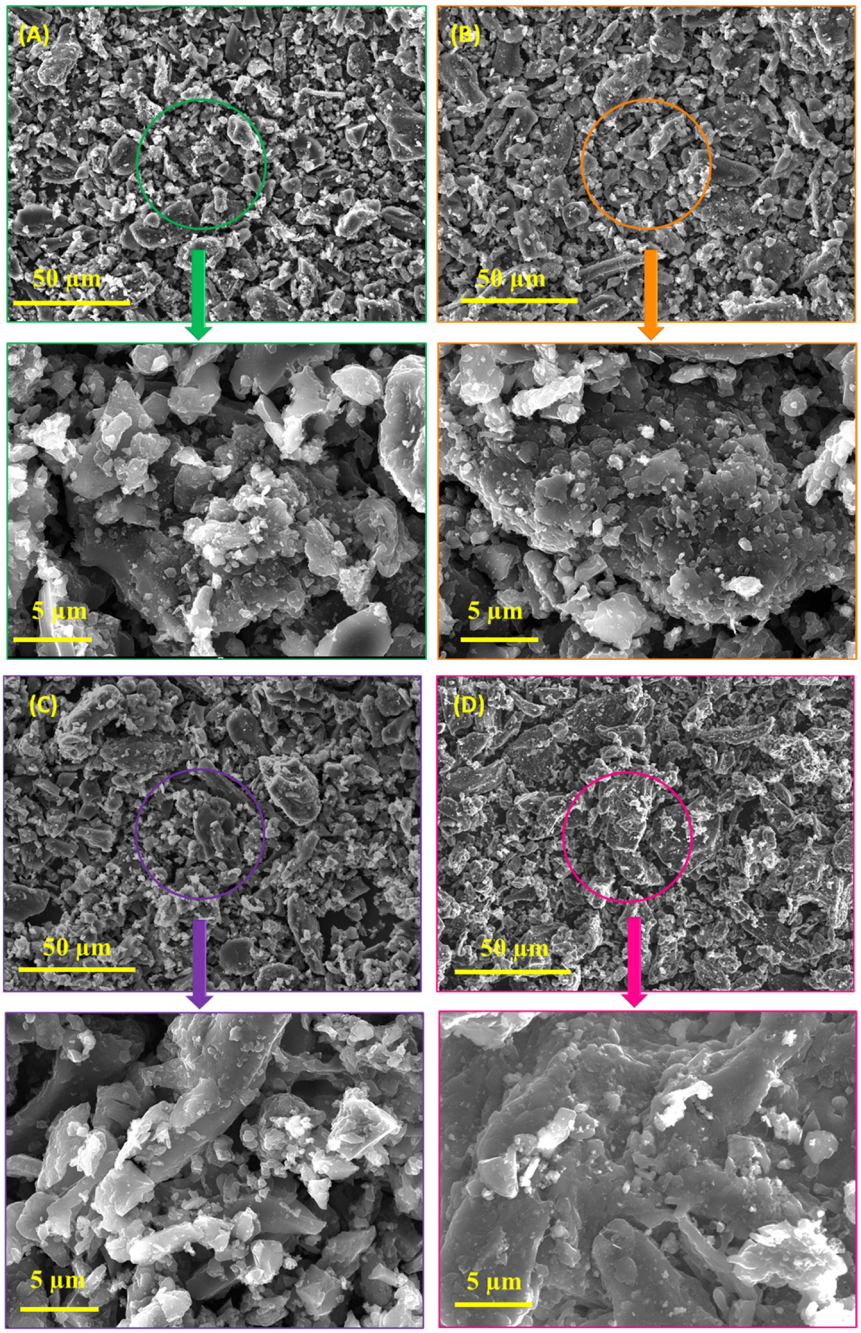

Fig. 2 SEM images and their magnifications of (A) HC-750 °C, (B) HC-1000 °C, (C) HC-1250 °C, and (D) OP-1250 °C.

1220–1180 cm^{-1} can be associated with the stretching vibration of P═O groups with hydrogen bonds, which is characteristic of phosphates or polyphosphates as well as the O–C stretching vibration in P–O–C bonds and P═OOH groups, present in the HC-750, HC-1000, HC-1250 °C samples but not found in the OP-1250 °C sample. Additionally, the band in the range of 727–800 cm^{-1} corresponds to C–P bond vibration.[38–40] This result agrees with quantitative identification of the chemical composition of the olive pomace after carbonization using EDX, and XRF was listed in terms of weight percentage (Tables S1 and S2†), indicating the presence of phosphorus species as the main observation after chemical activation pyrolysis.

By using SEM analysis, carbon samples (HCs) derived from OP are examined for their morphology and structure. Overall, the morphology of OP-R is distinguished by a compact surface without pores or curly structures, as shown in Fig. S4.† And, to better observe the effects of the chemical activation step and carbonization temperature on the HC morphology, SEM images are presented in Fig. 2A–D. These samples present an irregular granular morphology with particle sizes around 20–45 μm. Furthermore, the corresponding magnification images show that the HC surface is rough, with heterogeneous particle size distributions and pores of different diameters. These observations can be explained by the release of pyrolysis gas during

Open Access Article. Published on 10 June 2025. Downloaded on 1/23/2026 5:39:04 AM.
This article is licensed under a Creative Commons Attribution-NonCommercial 3.0 Unported Licence.

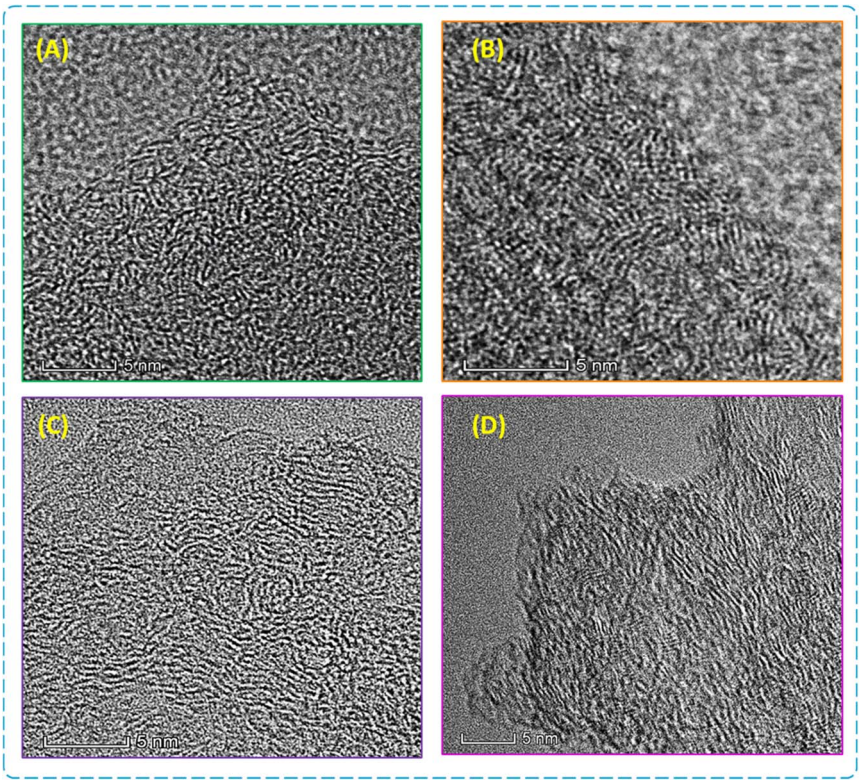

Fig. 3 HR-TEM images of HC samples synthesized at various temperatures. (A) HC-750 °C, (B) HC-1000 °C, (C) HC-1250 °C, and (D) OP-1250 °C.

high-temperature treatment, which causes the formation of porous structures.[25]

According to Fig. 3, the HR-TEM images showed that the carbons obtained are mainly composed of many layers of disordered carbon, which reveals a characteristic typical of amorphous carbon.[41] It is also possible to see a small number of parallel graphene sheets. At 750 °C, the HC has a predominantly amorphous structure with disordered carbon layers and an apparent lack of graphitization, indicating initial disordered carbon structures. At 1000 °C, a significant evolution is observed with the appearance of partially graphitic zones and increased surface roughness, indicating better organization of carbon structure. The HC-1250 °C sample shows a more organized structure, which is still a feature of HC, with longer and better-aligned carbon layers. However, the graphitization of OP-1250 °C (Fig. 3D) is less obvious than that of HC-1250 °C, suggesting that chemical activation increases graphitization. As the temperature of the heat treatment increases, the carbon layer

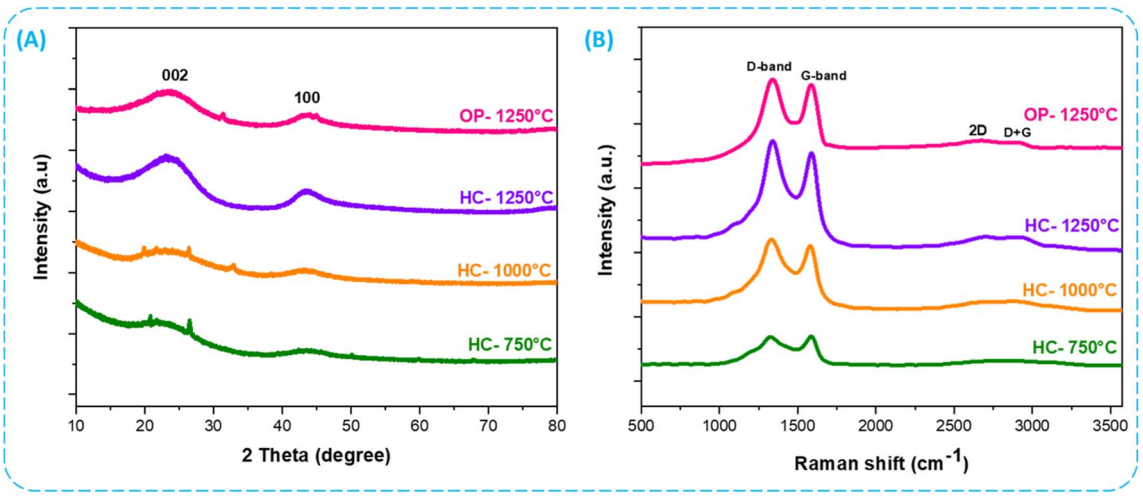

Fig. 4 (A) XRD and (B) Raman spectrums of HC samples for different temperatures.

© 2025 The Author(s). Published by the Royal Society of Chemistry

Open Access Article. Published on 10 June 2025. Downloaded on 1/23/2026 5:39:04 AM. This article is licensed under a Creative Commons Attribution-NonCommercial 3.0 Unported Licence.

Table 1 Physical parameters of hard carbon samples

Sample	2 Tetha	d_{002} (nm)	FWHM (rad)	L_c (nm)	L_a (nm)	N Layers	$A_{(D/G)}$	SBET ($m^2\ g^{-1}$)
HC-750 °C	23.27	0.395	7.87	10.429	21.061	2.722	1.798	172.87
HC-1000 °C	23.74	0.379	7.207	11.388	23.012	3.012	1.341	86.72
HC-1250 °C	23.78	0.373	6.382	12.871	25.975	3.451	1.318	7.094
OP-1250 °C	23.77	0.382	6.934	11.837	23.927	3.089	1.357	3.124

becomes longer. The crystalline zones' interlayer distances were found to be 0.51 nm for HC-750 °C, 0.49 nm for HC-1000 °C, and 0.44 nm for HC-1250 °C. These values exceed the required distance (0.37 nm) for sodium intercalation and follow the general trend that distances between layers decrease as pyrolysis temperatures increase.[42–44] The main components of HC in basic analysis are carbon (C) and oxygen (O), with the carbon content increasing as temperature increases, except for sample OP-1250 °C (Table S2 and Fig. S6†). We also observe that all HC samples contain phosphorus (P) traces, which decrease with increasing temperature. The presence of several heteroatoms can provide additional sites for sodium accommodation and improve electrolyte wettability, enhancing the sodium storage performance in HCs.[39,44] These observations show the important role that carbonization temperature plays in the morphology and internal structure of HC, highlighting the importance of heat treatment conditions to improve the properties of carbon materials.

Additionally, XRD (Fig. 4A) and Raman measurements (Fig. 4B) confirmed that the resulting HC is graphitized. The XRD diagrams showed that the hard carbon from olive pomace presents two peaks at 24° and 43°. This corresponds to the diffraction of the (002) and (100) planes of disordered carbon, respectively.[45] The (002) peaks shift to a higher diffraction angle when the carbonization temperature rises, and d_{002} decreases due to relative order increases. The d_{002} values are 0.395, 0.379, 0.373, and 0.382 nm at HC-750, HC-1000, HC-1250, or OP-1250 °C, significantly higher than graphite (0.335 nm). Other parameters are also evaluated from the XRD data, such as the average lateral length (L_a) and the thickness of graphite-like segments.[46] The number (N) of stacked graphene sheets is obtained as $N = L_c/d_{002}$ (Table 1). L_a, L_c, and N are expected to increase with temperature if a long-range order develops. The average lateral length increases rapidly and corresponds to the HR-TEM results.

Raman spectroscopy confirmed the development of the microcrystalline structure of graphite in HC, as shown in Fig. 4B. The Raman spectrum of carbon has two broad peaks in the range of 1100–1900 cm^{-1}, with narrow samples having well-ordered graphite networks, the G band situated at about 1580 cm^{-1} corresponds to the in-plane stretching vibrations of sp^2 carbon.[47,48] The D band was observed around 1350 cm^{-1}. This mode is inactive in full graphite, but it can be activated by structural disorders, defects, or heteroatom impurities.[39,48] Proportional strong D bands show that the HC-1000, HC-1250, and OP-1250 °C samples have numerous structural defects, which are considered to be significant sites for sodium storage in the carbon structure. The Lorentzian fit of the D and G peak areas of the Raman spectra is shown in Fig. S7.† To better assess the microcrystalline structure of the samples, the degree of graphitization of the carbon materials can be determined by analyzing the ratio of the integral area of the $A_{(D/G)}$.[44,46] The results of the peak fitting show that $A_{(D/G)}$ decreases with a temperature rise, from 1.74 for HC-750 °C to 1.31 for HC-1250 °C. Graphitic domain growth at higher carbonization temperatures is confirmed by the change in $A_{(D/G)}$ corresponding to previous XRD and HR-TEM above results. This indicates that the structure of the HC can be more graphitic and enhance

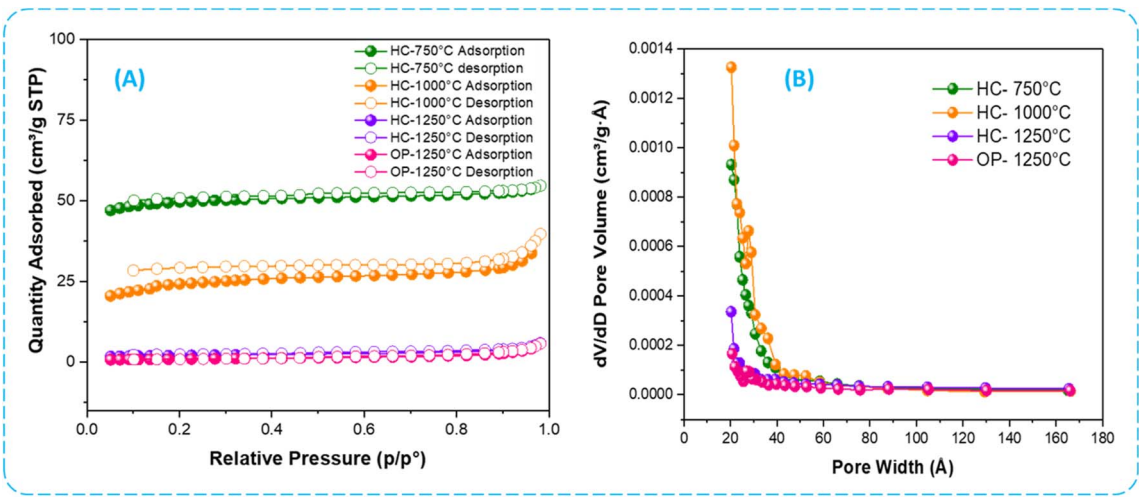

Fig. 5 (A) N_2 adsorption–desorption isothermal curves, and (B) pore size distribution of HC for different temperatures.

Open Access Article. Published on 10 June 2025. Downloaded on 1/23/2026 5:39:04 AM.
This article is licensed under a Creative Commons Attribution-NonCommercial 3.0 Unported Licence.

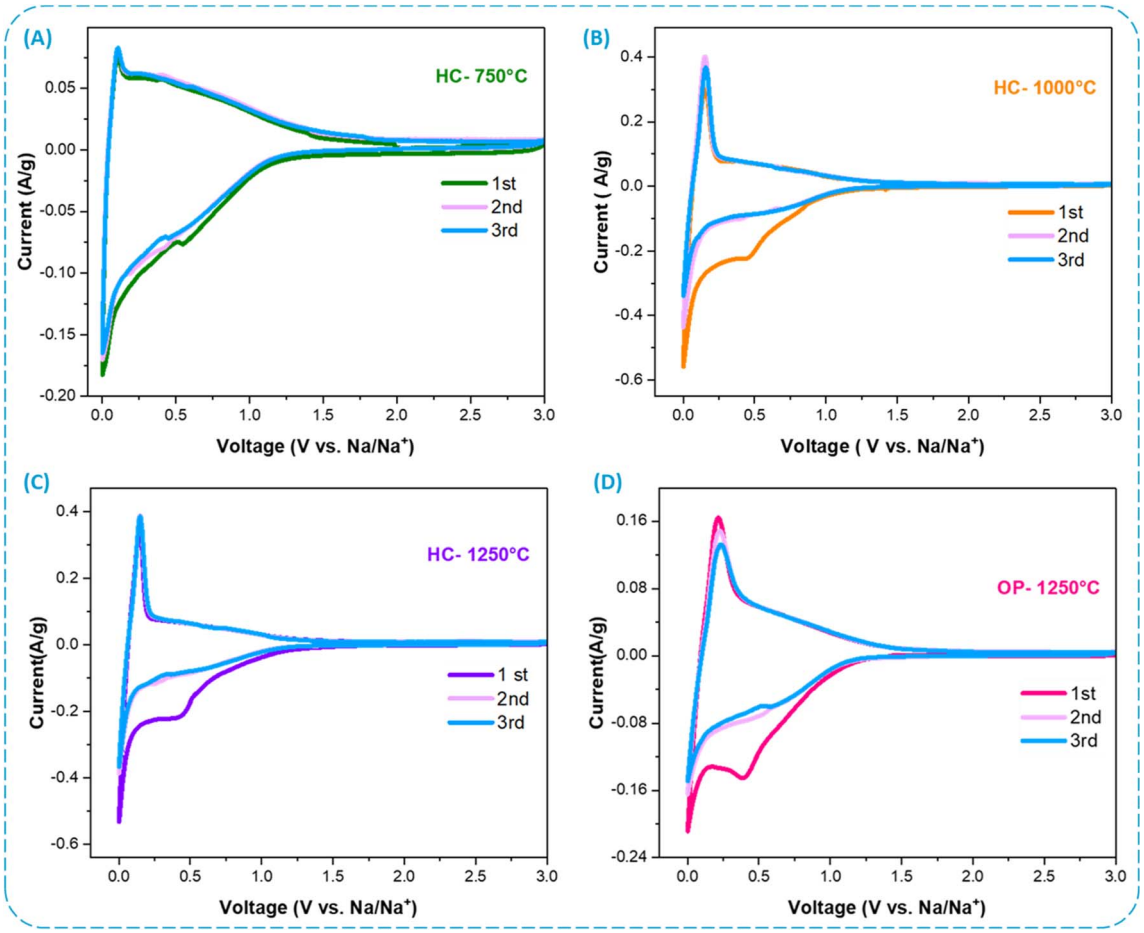

Fig. 6 CV curves at a scan rate of 0.1 mV s^{-1} of (A) HC-750, (B) HC-1000, (C) HC-1250, and (D) OP-1250 °C.

anode performance in terms of specific capacity and cycling stability.

To determine the BET specific surface area, Fig. 5A shows the N_2 adsorption–desorption isotherms of HC samples at different temperatures. The isotherms of HC were similar to type II, suggesting a low porosity of HC. The calculated S_{BET} are 172.87, 86.83, 7.09, and 3.12 m^2 g^{-1} of HC-750, HC-1000, HC-1250, and OP-1250 °C, respectively. This indicates that the specific surface area is directly related to the carbonization temperature. The calculated BET surface area decreases with increasing heat treatment temperature (Table 1). This low surface area of HC-1250 °C could induce limited formation of solid electrolyte interphase (SEI) and thus improve the initial Coulomb efficiency, which is consistent with the electrochemical results. Fig. 5B shows pore distribution with pore volume and diameter values for the various HCs obtained. As the temperature rises, the average pore diameter of the sample decreases pore volume. In combination with other analytical methods such as SEM and HR-TEM, this pattern can be explained by the fact that higher carbonization temperatures lead to micropore closure and eliminate structural flaws, which lowers the pore volume of HC obtained from biomass.

3.2. Electrochemical sodium storage performance

To investigate the performance of the electrochemical behavior of HC derived from OP as an anode for SIBs, the samples were transformed into working electrodes and assembled in CR2032-type coin cells. CV curves for HC samples treated at 750, 1000, and 1250 °C are displayed in Fig. 6A–C, these curves were recorded cycles at a scan rate of 0.1 mV s^{-1} in the first three cycles between 3 to 0 V. The first reduction peak that disappeared in the following cycle is related to the formation of a solid electrolyte interface (SEI) film and certain irreversible secondary reactions.[25,48] The second peak corresponds to the insertion of sodium into the carbon structure. Observed in the same manner as the first anodic scan, a peak below 0.1 V was observed, followed by a wide sloped region that is typical of sodium storage that can be reverted through intercalation and adsorption mechanisms on structural defects in the carbon.[49] Although the CV curves for different HC samples are similar, the redox peak is below 0.1 V, increases in amplitude with increasing calcination temperature, especially for the HC-1000 °C and HC-1250 °C samples. Based on this result, the Na storage mechanisms transition from primarily adsorption to primarily intercalation as the temperature rises, and the

© 2025 The Author(s). Published by the Royal Society of Chemistry

Open Access Article. Published on 10 June 2025. Downloaded on 1/23/2026 5:39:04 AM.
This article is licensed under a Creative Commons Attribution-NonCommercial 3.0 Unported Licence.

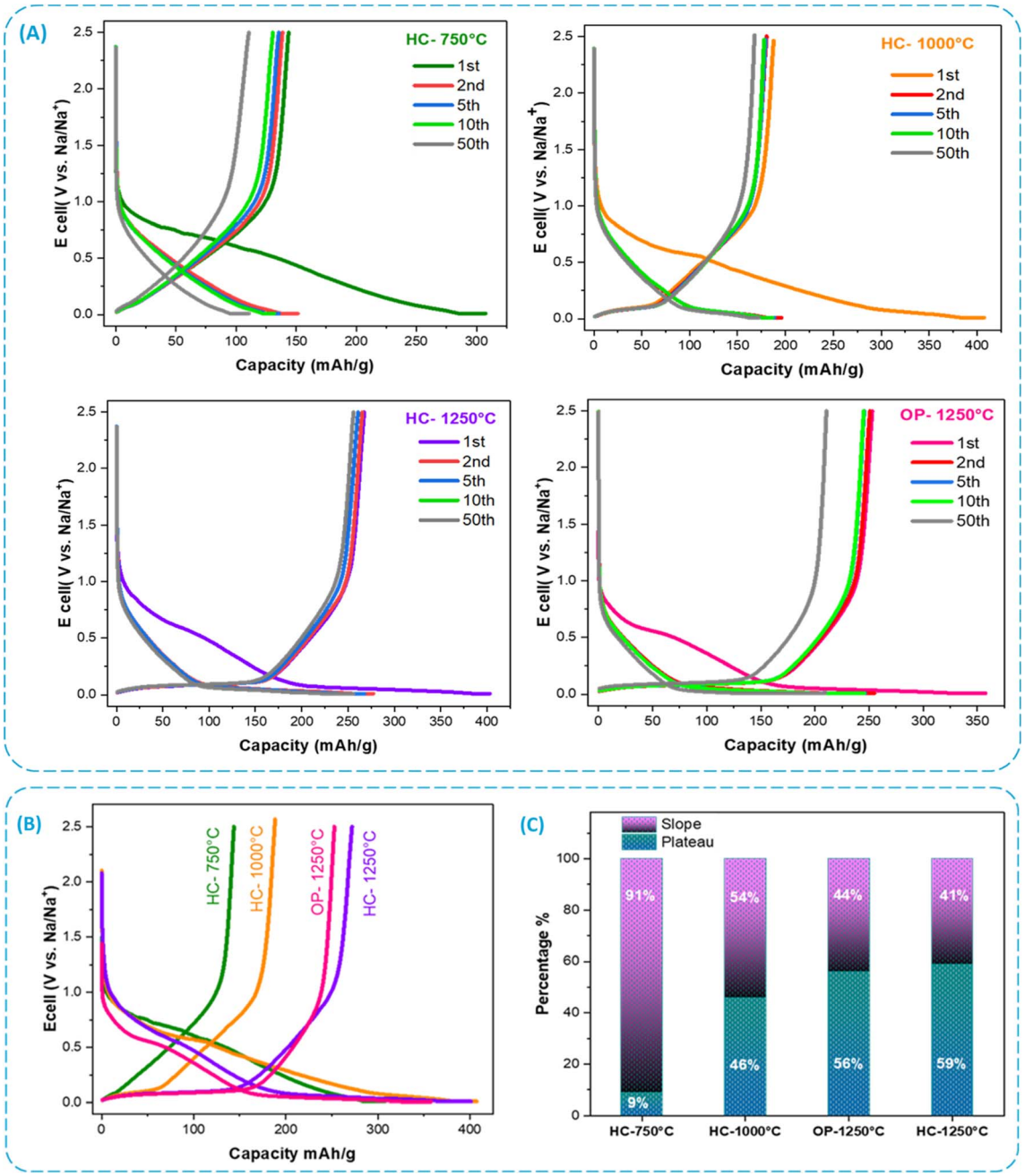

Fig. 7 (A) Galvanostatic charge/discharge curves of HC electrodes at 25 mA g^{-1}, (B) comparison of charge/discharge profiles of HC during the first cycle, and their (C) sloping and plateau capacity of each electrode at different temperatures.

reduction in interlayer spacing d_{002} is associated with facilitating sodium intercalation reactions.[44,46]

In order to verify the electrochemical stability of the electrodes for different temperatures, galvanostatic curves for HC at a constant current density of 25 mA g^{-1} over the voltage range of 0.01–2.5 V for 50 cycles are displayed in Fig. 7A. During the first cycle, the discharge capacity for HC-750, HC-1000, HC-1250, and OP-1250 °C was 307, 407, 403, and 358 mA h g^{-1}, respectively. A charge capacity of 146, 193, 272, and 253 mA h g^{-1} with initial coulombic efficiency (ICE) of 47%, 48%, 68%, and 70%, respectively, followed the sodiation process. Generally, the irreversible capacity loss observed in the initial cycle is due to the decomposition of the electrolyte and the formation of the SEI layer on the surface.[41] Based on the above results, including characterization of FT-IR, indicate that an increase in the capacity of the first-cycle of heat temperature rises the availability of the active sites of sodium. These active sites may correspond to defects, voids, and intermediate layers accessible to sodium with HC.[50,51] It has also been observed that the HC-1250 °C sample have a higher specific capacity than the HC-750 °C and HC-1000 °C samples. This due to the presence of microstructural properties that enhance storage capacity.

Open Access Article. Published on 10 June 2025. Downloaded on 1/23/2026 5:39:04 AM. This article is licensed under a Creative Commons Attribution-NonCommercial 3.0 Unported Licence.

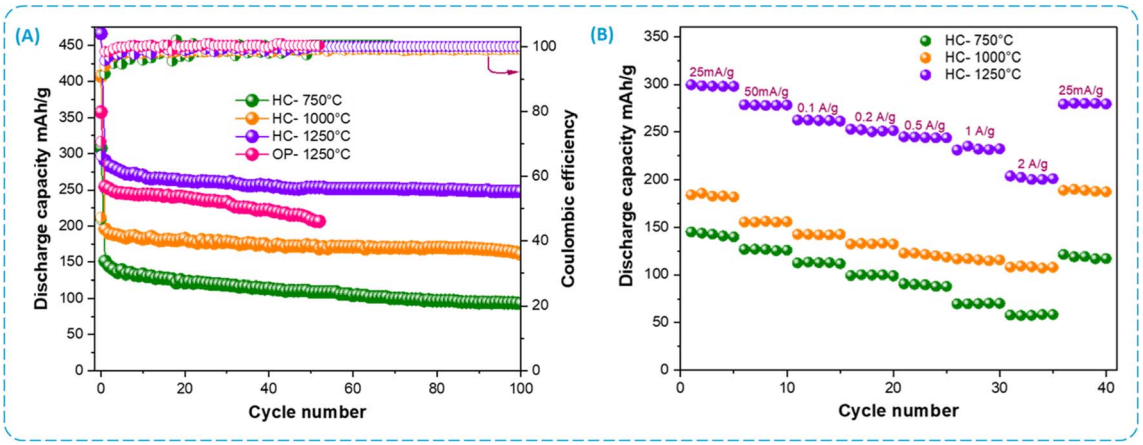

Fig. 8 Electrochemical performance of the HC electrodes at different temperatures (A) capacity retention and the coulombic efficiency, (B) rate performance at different current densities.

Table 2 Comparison of carbon HC-1250 °C storage performance with different hard carbons used as anode for SIBs

Samples	Current density (mA g^{-1})	Initial capacity (mA h g^{-1})	Cycle number	Keep capacity (mA h g^{-1})	CE %	Ref.
Seeds1400	25	274	10	—	88%	27
TC1600	20	203	100	197	66%	41
Argan-1300	25	360	70	278	86%	26
WHC900	30	371	50	240	71	49
MCS-24	100	545	200	250	47%	53
Hollow carbon	100	537	100	160	41.5%	54
HC-1250 °C	25	403	100	248	68%	This work

However, after the first cycle, all HC electrodes have high coulombic efficiency (CE) and good retention capacity. Thus, the CE of the electrode reaches 99% and 100% in the second cycle and remains stable afterwards. The improvement in cycling performance may be related to a decrease in the surface functional groups of carbon after high-temperature treatment.

The GCPL curves of the samples shown in Fig. 7B provide a better understanding of how Na^+ ions are inserted into carbon and how this mechanism develops as a function of carbonization temperatures. Based on the results of cyclic voltammetry (CV), the charge/discharge curves can be classified into two different zones. One that slopes above 0.1 V and one that plateaus below that value. It is widely known that the insertion storage mechanism of Na^+ ions varies significantly between these two regions. As shown in Fig. 7B, the plateau's capacity increases significantly with increasing carbonization temperature.[52] In contrast, the results show that for HC-750 °C, only a sloping region is observed without a low-potential plateau. This suggests that the capacity observed for HC-750 °C is mainly due to the adsorption of Na^+ ions onto active sites on the material surface.[51] Conversely, the electrodes of HC-1000, HC-1250, and OP-1250 °C exhibited not only a sloping region but also a plateau in the voltage range below 0.1 V. The charge capacity observed in the plateau region for HC-1000 °C is 76 mA h g^{-1}, representing around 46% of the total capacity. For HC-1250 °C, the plateau capacity rises to 168 mA h g^{-1}, representing 59% of the total capacity (Fig. 7C). These results are comparable to those of previous studies, which have demonstrated that the plateau regime rises with an increase in temperature.[41,51] Therefore, extending the plateau region may serve as an effective approach to improving the ICE in HC electrodes.[44] As the carbonization temperature rises, the spacing between the carbon layers decreases, which decreases the slope capacity. Conversely, an increase in the size of the nano-cavity leads to an increase in plateau capacity. This observation is confirmed by XRD analysis of hard carbon samples, which shows a decrease in the *d*-spacing with carbonization temperature rises.

At 25 mA g^{-1}, Fig. 8A presents the cycling performance of HC electrodes and OP-1250 °C electrode. After 100 cycles, the HC-1250 °C electrode displayed a reversible specific capacity of 248 mA h g^{-1}, with a CE around 99.9%. Whereas, HC-1000 and HC-750 °C retained capacity at 161 and 94 mA h g^{-1}, respectively. Furthermore, the OP-1250 °C electrode shows a significantly lower capacity and retention compared to the HC-1250 °C electrode. These results show that the HC-1250 °C electrode has a remarkable high performance, underline the importance of the chemical activation step and the carbonization temperature in the process to produce hard carbon derived from olive pomace, and are in good agreement with the porous structure and active sites in the resulting carbon material. Table 2 presents a list of hard carbons from biomass and mentioned in the

© 2025 The Author(s). Published by the Royal Society of Chemistry

Open Access Article. Published on 10 June 2025. Downloaded on 1/23/2026 5:39:04 AM.
This article is licensed under a Creative Commons Attribution-NonCommercial 3.0 Unported Licence.

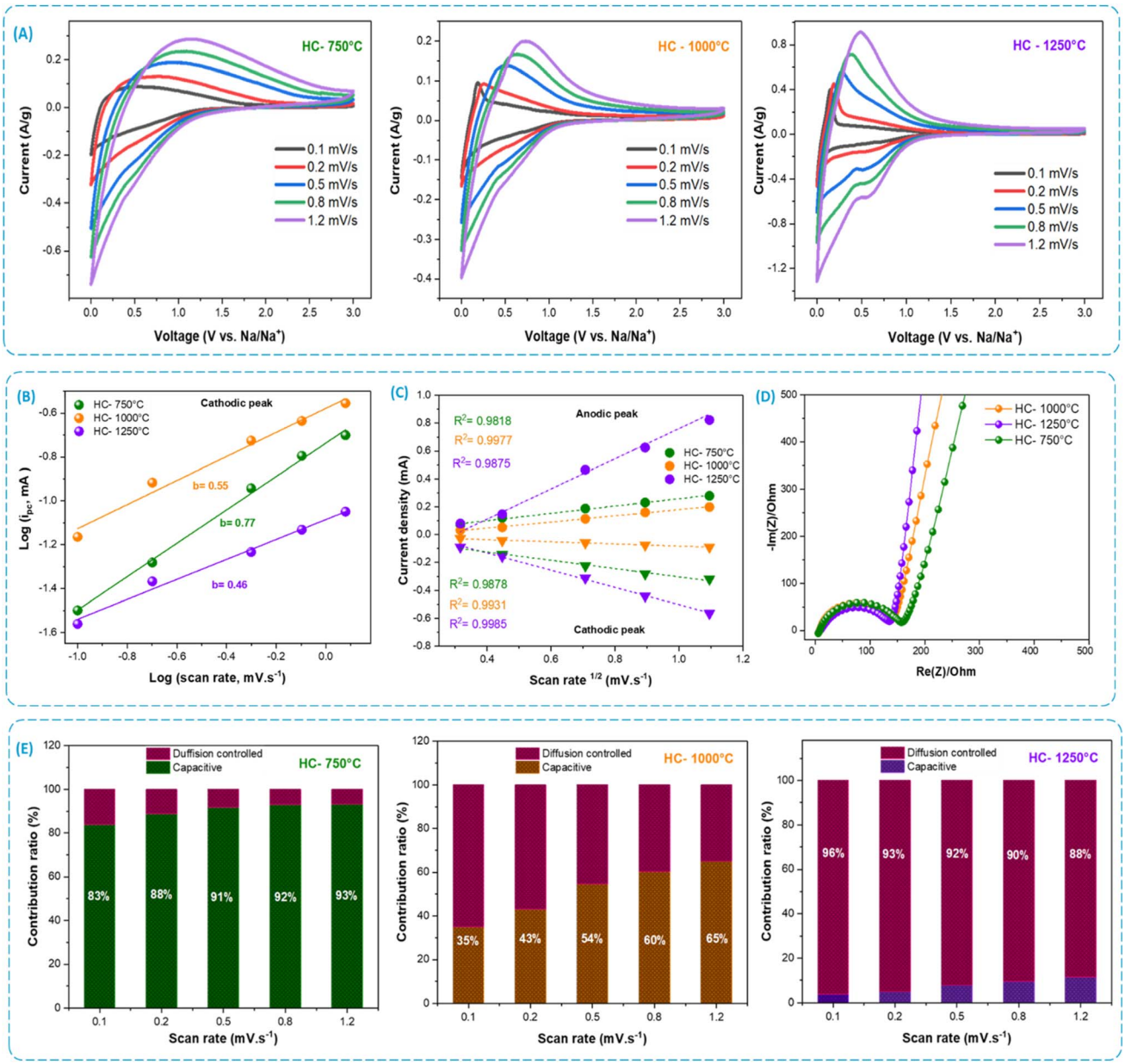

Fig. 9 (A) CV curves at various scan rates from 0.1 to 1.2 mV s^{-1}, (B) linear relationship between log(*i*) *vs.* log(*v*) for the samples, (C) linear relation between peak current *ip* and the square root of various scan rate $v^{1/2}$, (D) impedance spectroscopy of the samples, (E) the capacity contribution at various scan rates.

literature used as anode for sodium-ion batteries. Some have superior or similar performances in terms of cycles and cycles and CE%. However, this often involves complex processes, long times and very high carbonization temperatures (>1300 °C).[26,27,41] Fig. 8B displays the rate performance of HC electrodes with currant densities ranging from 25 to 2000 mA g^{-1} then returning to 25 mA g^{-1}. It may be observed that HC-1250 °C not only has the highest specific capacitance at a low current density of 25 mA g^{-1}, but also has the best electrochemical rate performance compared to HC-750 °C and HC-1000 °C. Charge capacities of 146, 194, and 282 mA h g^{-1} at 25 mA g^{-1} are delivered for the HC-750, HC-1000, and HC-1250 °C electrodes, respectively. In addition, at a higher current density of 2000 mA g^{-1}, these electrodes have capacities of 54, 115 and 224 mA h g^{-1}, respectively. As soon as the current density gradually decreases to 25 mA g^{-1} after cycling at 2000 mA g^{-1}, the electrodes may return to higher capacities than initially found. This confirms excellent rate capability of the HC electrodes, especially the HC-1250 °C electrode, indicating the remarkable stability of the structure during charge/discharge processes. The properties of HC electrodes are determined by their electronic conductivity and their ability to intercalate sodium ions.[49] Increasing the temperature of carbonization can enhance the electronic conductivity of the electrode material. However, at higher

Open Access Article. Published on 10 June 2025. Downloaded on 1/23/2026 5:39:04 AM.
This article is licensed under a Creative Commons Attribution-NonCommercial 3.0 Unported Licence.

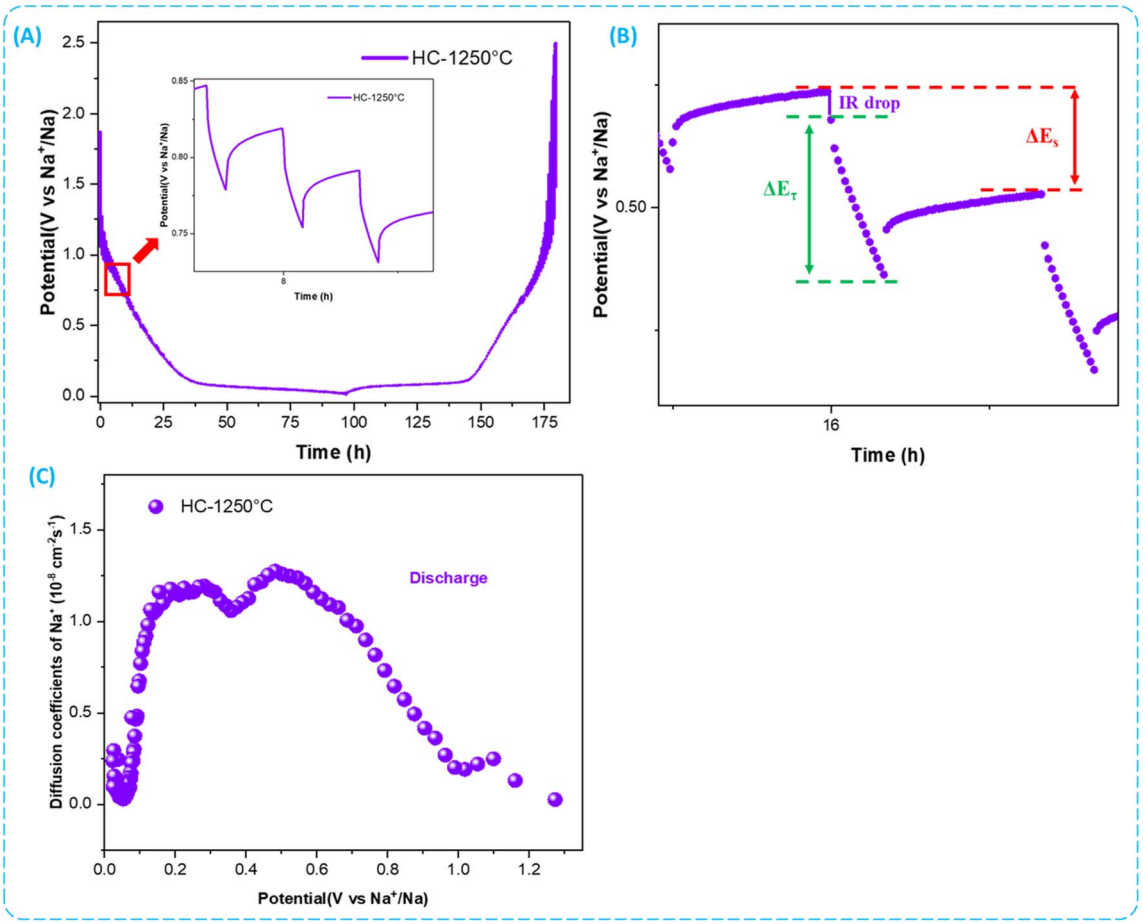

Fig. 10 (A) The GITT curves of HC-1250 °C, (B) potential profile of constant current pulse with schematic labeling of different parameters, (C) D_{Na^+} diffusion coefficients calculated from the GITT for discharge process.

current rates, the capacitance decreases because of the plateau region's reduced contribution.[41,52]

To assess the electrochemical performance of HC derived from the OP, cyclic voltammetry analysis was conducted with various scan rates of 0.1 to 1.2 mV s^{-1}. The resulting CV curves (Fig. 9A) provide insights into the sodium-ion storage mechanisms within different HC structures. Typically, sodium storage behavior can be categorized into two components: (i) a fast reaction governed by capacitive processes and (ii) a slower battery-like reaction. By using the eqn (1),[44,55] it is possible to distinguish between these two energy storage mechanisms:

$$i = a \times v^b \quad (1)$$

where i is the current density, v is the scan rate, and a and b are variables. The transformation allows you to obtain the following eqn (2):

$$\log(i) = b \times \log(v) + \log(a) \quad (2)$$

The value of the slope (b) is used to determine the sodium storage mechanism. If the value of b is close to 0.5, this means that the process is controlled by diffusion. This corresponds to the storage of sodium due to a battery-type reaction with slow kinetics. Conversely, a b value close to 1 suggests that sodium storage is mainly dominated by a fast capacitive mechanism.[56] As presented in Fig. 9B, the downward peaks in the discharge part, referred to as the reducer peaks, and the plots of log(i) *versus* log(v), provide insight into the storage mechanism. The values of b determined for samples HC-750, HC-1000, and HC-1250 °C electrodes were 0.77, 0.55, and 0.46, respectively. These values indicate the transition from a predominantly capacitive mechanism for HC-750 °C to a combined capacitive and diffusion-controlled mechanism for HC-1000 and HC-1250 °C. This suggests that as the carbonization temperature increases, the sodium storage mechanism shifts towards a more diffusion-controlled process, improving the intercalation of sodium ions.

The equation below (3) can be used to determine the contribution of capacitive or intercalation processes to a fixed potential.[57]

$$i(v) = k_1 v + k_2 v^{1/2} \quad (3)$$

where $i(v)$ is the current at a given potential V, $k_1$and k_2 are constants. The $k_1 v$ part represents the capacitive contribution, while $k_2 v^{1/2}$ represents the diffusive contribution. By plotting $i(v)/v^{1/2}$ as a function of $v^{1/2}$, we obtain k_1 as the intercept and k_2 as the slope. Fig. 9C shows a plot based on eqn (3) at constant

© 2025 The Author(s). Published by the Royal Society of Chemistry

Open Access Article. Published on 10 June 2025. Downloaded on 1/23/2026 5:39:04 AM.
This article is licensed under a Creative Commons Attribution-NonCommercial 3.0 Unported Licence.

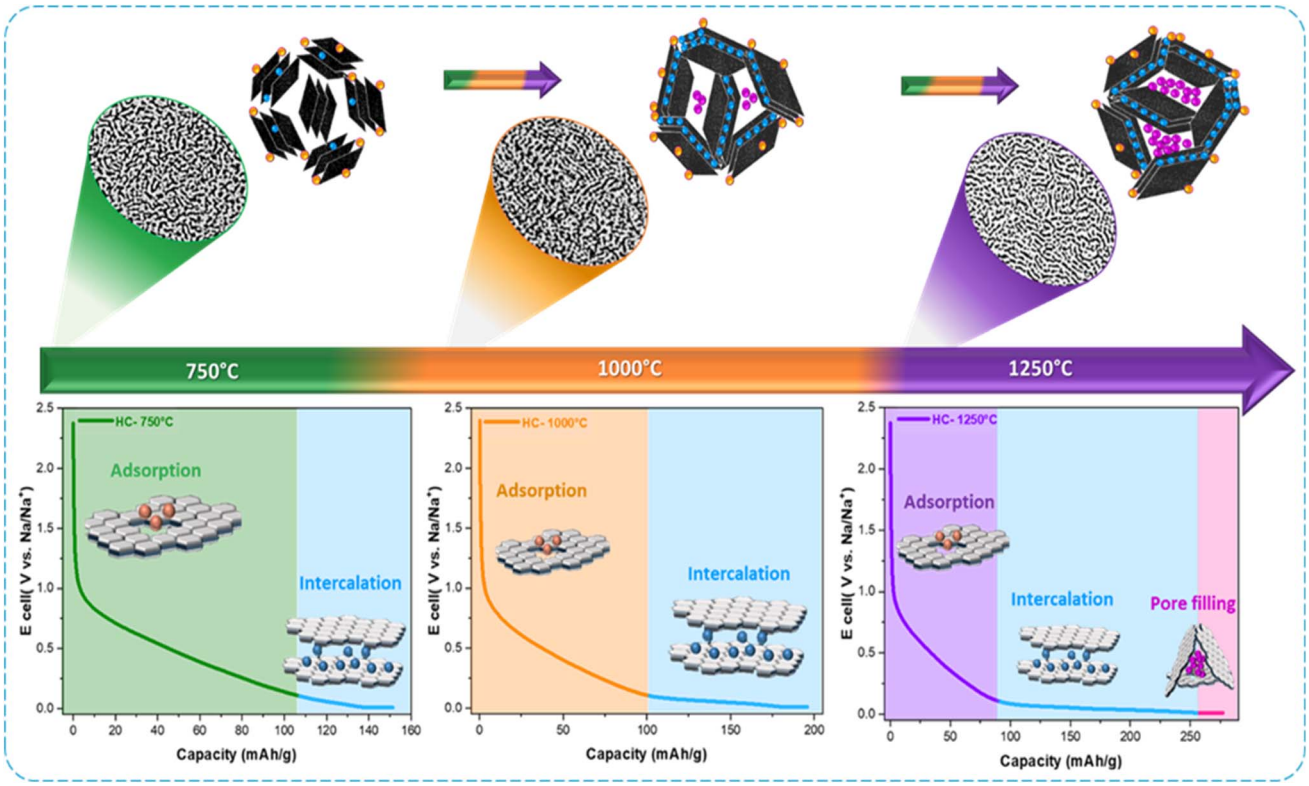

Fig. 11 Schematic illustration of how sodium ions are stored in hard carbons derived from olive pomace at various carbonization temperatures.

potential. The plots of the anodic and cathodic scans are almost linear, with an R^2 value close to unity greater than 98%. The values of k_1 and k_2 were obtained at each particular potential to calculate the capacitive and diffusive currents. By using this analysis, we can determine the proportion of each mechanism in the sodium storage process. Fig. 9E provides a quantitative analysis of the contribution to the capacity of hard carbons as a function of increasing scan speed. The results show that the HC-750 °C sample, characterized by a capacitive contribution, is predominant (83–93%), indicating a storage mechanism primarily by surface adsorption. In contrast, for HC-1000 °C, the diffusion contribution increases with carbonization temperature, reaching 65%, suggesting a mixed mechanism between capacitive and diffusion contribution. For HC-1250 °C, the diffusion contribution is dominant (88–96%), suggesting that the intercalation of sodium ions into the carbon structure is primarily responsible for controlling the storage mechanism.

In order to investigate how carbonization temperature affects the electrochemical properties of HC. Fig. 9D shows the Nyquist plots of impedance spectrums that are generally composed of a semicircle in the high-frequency region and a sloped straight line in the middle and low-frequency zones. These features may be attributed to the charge transfer resistance (R_{ct}) and Warburg impedance (W_o) associated with Na^+ ion diffusion in carbonized materials.[49] For all composite electrodes, as the carbonization temperature increases, there is a slight decrease in charge transfer resistance (R_{ct}). The HC-1250 °C sample shows the lowest R_{ct} value (130 Ω) compared to the HC-1000 °C (139 Ω) and HC-750 °C (157 Ω) electrodes. A lower R_{ct} indicates faster electrochemical reaction kinetics. These results highlight the importance of optimizing carbonization temperature to improve the electrochemical properties and performance of HC anodes for SIBs.

Galvanostatic intermittent titration (GITT) was used to measure the diffusion coefficient of sodium ions to better understand the storage mechanisms of sodium ions. Fig. 10A shows the GITT curves of H-1250 °C. In the GITT tests, sodiation and desodiation were carried out at a constant current density of 20 mA g^{-1}. The diffusion coefficient was calculated according to Fick's second law (eqn (4)):

$$D_{Na^+} = \frac{4}{\pi\tau}\left(\frac{m_b V_m}{M_B A}\right)^2 \left(\frac{\Delta E_s}{\Delta E_\tau}\right)^2 \quad (4)$$

where τ (s), m_B (g), V_M (cm^3 mol^{-1}), M_B (g mol^{-1}), and S (m^2 g^{-1}) are the pulse duration, active mass of the electrode, molar volume, molecular weight, and active surface area of the electrode, respectively. Additionally, ΔE_S and ΔE_τ are obtained from the GITT curves (Fig. 10B). Based on these results, the sodium storage behavior can be divided into two regions: a low-potential plateau and a high-potential slope. The sodium ion diffusion coefficient D_{Na^+} of HC-1250 °C is in the order of 10^{-8} cm^2 s^{-1} during the discharge processes, as shown in Fig. 10C. These found values indicate good transport kinetics of Na^+ ions in HC-1250 °C hard carbon derived from olive pomace, confirming that the optimization of the carbon structure at high temperature significantly improves the electrochemical

Open Access Article. Published on 10 June 2025. Downloaded on 1/23/2026 5:39:04 AM. This article is licensed under a Creative Commons Attribution-NonCommercial 3.0 Unported Licence.

performances, in particular by facilitating the rapid insertion of sodium ions into the interstices of the carbon.

In summary, the sodium storage mechanism of HC samples made from OP differs depending on the carbonization temperature, highlighting the adsorption, intercalation, and pore-filling mechanisms (Fig. 11). For HC-750 °C, the sodium storage mechanism is mainly dominated by surface adsorption. This is indicated by the predominance of a steep slope in the discharge/charge curves. This indicates that sodium ions mainly bind to active sites on the carbon surface without penetrating deeply into the structure. As the temperature increases to 1000 °C (HC-1000 °C), the storage mechanism transitions to a combination of adsorption and intercalation. The GCPL curves display both a sloping region and a plateau at low potential, suggesting that sodium ions begin to intercalate between carbon layers while still binding to surface sites. This shift is facilitated by an improved structural organization of the carbon, enhancing its storage capacity. For HC-1250 °C, the storage mechanism is mainly dominated by sodium ion intercalation. GCPL curves reveal a well-defined plateau at low potential, characteristic of intercalation, where sodium ions penetrate the interstices between carbon layers. TEM and XRD analyses of HC-1250 °C confirm this ordered structure with well-defined carbon layers, favoring intercalation and pore filling. As the carbonization temperature increases, the spacing between the carbon layers decreases, which facilitates the intercalation of sodium ions and thus increases storage capacity.

4. Conclusion

In conclusion, the present investigation elucidates the significant potential of hard carbon derived from olive pomace as a highly effective anode material for sodium-ion batteries. The HC was synthesized and characterized at various carbonization temperatures. The findings indicate that the optimization of both carbonization temperature and chemical activation is imperative for enhancing the electrochemical performance of the resultant HC. A variety of analytical techniques, including Scanning Electron Microscopy (SEM), High-Resolution Transmission Electron Microscopy (HR-TEM), X-ray Diffraction (XRD), Raman spectroscopy, and Brunauer–Emmett–Teller (BET) surface area analysis, were utilized to thoroughly characterize the structure and morphology of the samples. Based on the outcomes from XRD and Raman spectroscopy, it can be concluded that the carbonization temperature effectively reduces the interlayer spacing, thereby facilitating sodium-ion intercalation. The electrochemical evaluations were particularly definitive for the HC synthesized at 1250 °C, which exhibited exceptional performance, achieving a discharge capacity of 403 mA h g^{-1} and an Initial coulombic Efficiency (ICE) of 68%. The HC-1250 °C sample exhibited a specific capacity of 248 mA h g^{-1} after 100 cycles, in contrast to the HC-1000 °C and HC-750 °C samples, which recorded capacities of 161 and 94 mA h g^{-1}, respectively. These results signify that the HC-1250 °C sample possesses remarkable cyclic stability and substantial energy storage capacity. A notable emphasis of this research resides in the straightforward nature of the synthesis process. This procedure encompasses the chemical activation of olive pomace using an H_3PO_4 solution, which engenders phosphorus doping within the carbonaceous material, followed by subsequent thermal carbonization. By adopting this approach, the waste generated from olive residues can be valorized and transformed into efficient materials for energy storage applications.

5. Future perspectives

It is evident that anode materials, such as graphene or silicon-based composites, possess exceptional electrochemical properties that make them more suitable for lithium-ion batteries. Nonetheless, they might not be the most efficient way to advance sodium-ion battery technology. As an alternative, hard carbon derived from olive pomace is a potential candidate as a commercial anode material for sodium-ion batteries due to its favorable electrochemical properties and structural stability. And contribute to the advancement of sustainable battery technologies and promote the circular economy by valorizing agricultural waste. The findings underscore the viability of using olive pomace, a readily available and carbon-rich byproduct, in the synthesis of hard carbon, which exhibits favorable electrochemical properties and structural integrity. Future research should focus on evaluating the electrochemical performance of the HC obtained in the assembly of a full cell and exploring carbon materials made from cellulose or lignin produced from olive pomace.

Data availability

Datasets will be made available on request.

Author contributions

Material preparation, data collection, and analysis were performed by IA. Investigation analysis by MA, and AC. The review and editing of the manuscript are carried out by MA, MD, and DM. Project administration and supervision, funding acquisition by MYA, and DM. All authors read and approved the final manuscript.

Conflicts of interest

The authors have no competing interests to declare that are relevant to the content of this article.

Acknowledgements

The authors are grateful to the editor and anonymous reviewers for their comments and constructive suggestions to improve the quality of this manuscript.

References

1 Z. Wang, Y. Li, Q. Zhou, Q. Li, R. Zhao, Z. Qiu, R. Zhang, Y. Sun, F. Wu, C. Wu, *et al.*, Multi-Ion Strategies Toward

 © 2025 The Author(s). Published by the Royal Society of Chemistry

Open Access Article. Published on 10 June 2025. Downloaded on 1/23/2026 5:39:04 AM. This article is licensed under a Creative Commons Attribution-NonCommercial 3.0 Unported Licence.

Advanced Rechargeable Batteries: Materials, Properties, and Prospects, *Adv. Energy Mater.*, 2024, **5**, 0109.
2 P. Wang, X. Zhu, Q. Wang, X. Xu, X. Zhou and J. Bao, Kelp-derived hard carbons as advanced anode materials for sodium-ion batteries, *J. Mater. Chem. A*, 2017, **5**(12), 5761–5769.
3 L. Liu, L. Xiao, Z. Sun, S. Bashir, R. Kasi, Y. Gu and R. T. Subramaniam, Rational manipulation of electrolyte to induce homogeneous SEI on hard carbon anode for sodium-ion battery, *J. Energy Chem.*, 2024, **94**, 414–429.
4 G. Shen, B. Li, Y. Xu, X. Chen, S. Katiyar, L. Zhu, L. Xie, Q. Han, X. Qiu, X. Wu and X. Cao, Waste biomass garlic stem-derived porous carbon materials as high-capacity and long-cycling anode for lithium/sodium-ion batteries, *J. Colloid Interface Sci.*, 2024, **653**, 1588–1599.
5 L. M. Zhu, G. C. Ding, Q. Han, Y. X. Miao, X. Li, X. L. Yang, L. Chen, G. K. Wang, L. L. Xie and X. Y. Cao, Enhancing electrochemical performances of small quinone toward lithium and sodium energy storage, *Rare Met.*, 2022, **41**, 425–437.
6 J. F. Peters, A. Peña Cruz and M. Weil, Exploring the economic potential of sodium-ion batteries, *Batteries*, 2019, **5**(1), 10.
7 K. M. Abraham, How comparable are sodium-ion batteries to lithium-ion counterparts?, *ACS Energy Lett.*, 2020, **5**(11), 3544–3547.
8 C. Vaalma, D. Buchholz, M. Weil and S. Passerini, A cost and resource analysis of sodium-ion batteries, *Nat. Rev. Mater.*, 2018, **3**(4), 1–11.
9 S. Komaba, Sodium-driven rechargeable batteries: an effort towards future energy storage, *Chem. Lett.*, 2020, **49**(12), 1507–1516.
10 L. Rakhymbay, N. Bazybek, K. Kudaibergenov, S. T. Myung, Z. Bakenov and A. Konarov, Present development and future perspectives on biowaste-derived hard carbon anodes for room temperature sodium-ion batteries, *J. Power Sources*, 2024, **602**, 234347.
11 H. Zhang, I. Hasa and S. Passerini, Beyond insertion for Na-ion batteries: nanostructured alloying and conversion anode materials, *Adv. Energy Mater.*, 2017, **8**(17), 1702582.
12 C. Wu, Y. Yang, Y. Zhang, H. Xu, X. He, X. Wu and S. Chou, Hard carbon for sodium-ion batteries: progress, strategies and future perspective, *Chem. Sci.*, 2024, **15**(17), 6244–6268.
13 S. Y. Hong, Y. Kim, Y. Park, A. Choi, N. S. Choi and K. T. Lee, Charge carriers in rechargeable batteries: Na ions vs. Li ions, *Energy Environ. Sci.*, 2013, **6**(7), 2067–2081.
14 M. D. Slater, D. Kim, E. Lee and C. S. Johnson, Sodium-ion batteries, *Adv. Funct. Mater.*, 2013, **23**(8), 947–958.
15 Z. Tang, R. Zhang, H. Wang, S. Zhou, Z. Pan, Y. Huang, D. Sun, Y. Tang, X. Ji, K. Amine and M. Shao, Revealing the closed pore formation of waste wood-derived hard carbon for advanced sodium-ion battery, *Nat. Commun.*, 2023, **14**(1), 6024.
16 M. S. Balogun, Y. Luo, W. Qiu, P. Liu and Y. Tong, A review of carbon materials and their composites with alloy metals for sodium ion battery anodes, *Carbon*, 2016, **98**, 162–178.
17 Y. Mei, Y. Huang and X. Hu, Nanostructured Ti-based anode materials for Na-ion batteries, *J. Mater. Chem. A*, 2016, **4**(31), 12001–12013.
18 Y. Kim, K. H. Ha, S. M. Oh and K. T. Lee, High-capacity anode materials for sodium-ion batteries, *Chem.–Eur. J.*, 2014, **20**(38), 11980–11992.
19 S. P. Ong, V. L. Chevrier, G. Hautier, A. Jain, C. Moore, S. Kim, X. Ma and G. Ceder, Voltage, stability and diffusion barrier differences between sodium-ion and lithium-ion intercalation materials, *Energy Environ. Sci.*, 2011, **4**(9), 3680–3688.
20 T. Wang, D. Su, D. Shanmukaraj, T. Rojo, M. Armand and G. Wang, Electrode materials for sodium-ion batteries: considerations on crystal structures and sodium storage mechanisms, *Electrochem. Energy Rev.*, 2018, **1**, 200–237.
21 X. Wu, Y. Chen, Z. Xing, C. W. K. Lam, S. S. Pang, W. Zhang and Z. Ju, Advanced carbon-based anodes for potassium-ion batteries, *Adv. Energy Mater.*, 2019, **9**(21), 1900343.
22 W. Lv, F. Wen, J. Xiang, J. Zhao, L. Li, L. Wang, Z. Liu and Y. Tian, Peanut shell derived hard carbon as ultralong cycling anodes for lithium and sodium batteries, *Electrochim. Acta*, 2015, **176**, 533–541.
23 J. Xiang, W. Lv, C. Mu, J. Zhao and B. Wang, Activated hard carbon from orange peel for lithium/sodium ion battery anode with long cycle life, *J. Alloys Compd.*, 2017, **701**, 870–874.
24 P. C. Rath, J. Patra, H. T. Huang, D. Bresser, T. Y. Wu and J. K. Chang, Carbonaceous Anodes Derived from Sugarcane Bagasse for Sodium-Ion Batteries, *ChemSusChem*, 2019, **12**(10), 2302–2309.
25 L. Pei, H. Cao, L. Yang, P. Liu, M. Zhao, B. Xu and J. Guo, Hard carbon derived from waste tea biomass as high-performance anode material for sodium-ion batteries, *Ionics*, 2020, **26**, 5535–5542.
26 M. Dahbi, M. Kiso, K. Kubota, T. Horiba, T. Chafik, K. Hida, T. Matsuyama and S. Komaba, Synthesis of hard carbon from argan shells for Na-ion batteries, *J. Mater. Chem. A*, 2017, **5**(20), 9917–9928.
27 I. Izanzar, M. Dahbi, M. Kiso, S. Doubaji, S. Komaba and I. Saadoune, Hard carbons issued from date palm as efficient anode materials for sodium-ion batteries, *Carbon*, 2018, **137**, 165–173.
28 B. Lu, C. Lin, H. Xiong, C. Zhang, L. Fang, J. Sun, Z. Hu, Y. Wu, X. Fan, G. Li and J. Fu, Hard-carbon negative electrodes from biomasses for sodium-ion batteries, *Molecules*, 2023, **28**(10), 4027.
29 Z. T. Liu, T. H. Hsieh, C. W. Huang, M. L. Lee and W. R. Liu, Temperature effects on hard carbon derived from sawdust as anode materials for sodium ion batteries, *J. Taiwan Inst. Chem. Eng.*, 2024, **154**, 104889.
30 N. Zhang, Q. Liu, W. Chen, M. Wan, X. Li, L. Wang, L. Xue and W. Zhang, High capacity hard carbon derived from lotus stem as anode for sodium ion batteries, *J. Power Sources*, 2018, **378**, 331–337.
31 H. Tao, L. Xiong, S. Du, Y. Zhang, X. Yang and L. Zhang, Interwoven N and P dual-doped hollow carbon fibers/

Open Access Article. Published on 10 June 2025. Downloaded on 1/23/2026 5:39:04 AM. This article is licensed under a Creative Commons Attribution-NonCommercial 3.0 Unported Licence.

graphitic carbon nitride: an ultrahigh capacity and rate anode for Li and Na ion batteries, *Carbon*, 2017, **122**, 54–63.
32 A. Kano, T. Okano, N. Hojo, S. Ito, M. Fujimoto and K. Nakura, New carbon materials with large closed pore volume for the anode of high energy Na-ion batteries, *ECS Meet. Abstr.*, 2016, **230**(5), 668.
33 M. M. Parascanu, M. P. Gamero, P. Sánchez, G. Soreanu, J. L. Valverde and L. Sanchez-Silva, Life cycle assessment of olive pomace valorization through pyrolysis, *Renew. Energy*, 2018, **122**, 589–601.
34 B. Alonso-Farinas, A. Oliva, M. Rodríguez-Galán, G. Esposito, J. F. García-Martín, G. Rodríguez-Gutiérrez, A. Serrano and F. G. Fermoso, Environmental assessment of olive mill solid waste valorization via anaerobic digestion versus olive pomace oil extraction, *Processes*, 2020, **8**, 626.
35 I. Alouiz, M. Benhadj, E. Dahmane, M. Sennoune, M. Y. Amarouch and D. Mazouzi, Elaboration of fibrous structured activated carbon from olive pomace via chemical activation and low-temperature pyrolysis, *Heliyon*, 2024, **10**(20), e38886.
36 S. W. Han, D. W. Jung, J. H. Jeong and E. S. Oh, Effect of pyrolysis temperature on carbon obtained from green tea biomass for superior lithium ion battery anodes, *Chem. Eng. J.*, 2014, **254**, 597–604.
37 J. Zhao, L. Yu, F. Zhou, H. Ma, K. Yang and G. Wu, Synthesis and characterization of activated carbon from sugar beet residue for the adsorption of hexavalent chromium in aqueous solutions, *RSC Adv.*, 2021, **11**(14), 8025–8032.
38 M. Sarkar, R. Hossain and V. Sahajwalla, Hard carbons from automotive shredder residue (ASR) as potential anode active material for sodium ion battery, *J. Power Sources*, 2023, **584**, 233577.
39 I. Alouiz, M. Aqil, M. Dahbi, M. Y. Amarouch and D. Mazouzi, Performance of high-energy storage activated carbon derived from olive pomace biomass as an anode material for sustainable lithium-ion batteries, *Resour. Chem. Mater.*, 2025, **4**(2), DOI: **10.1016/j.recm.2024.11.001**.
40 F. Cherdoud, S. Khelifi and A. Reffas, Activated carbons developed from Algerian agro-waste of palm trunk fiber: Characterization and adsorptive capacity for azo dyes removal, *Desalination Water Treat.*, 2023, **311**, 118–134.
41 Y. Li, M. P. Paranthaman, K. Akato, A. K. Naskar, A. M. Levine, R. J. Lee, S. O. Kim, J. Zhang, S. Dai and A. Manthiram, Tire-derived carbon composite anodes for sodium-ion batteries, *J. Power Sources*, 2016, **316**, 232–238.
42 B. Xiao, T. Rojo and X. Li, Hard carbon as sodium-ion battery anodes: progress and challenges, *ChemSusChem*, 2019, **12**(1), 133–144.
43 Y. Cao, L. Xiao, M. L. Sushko, W. Wang, B. Schwenzer, J. Xiao, Z. Nie, L. V. Saraf, Z. Yang and J. Liu, Sodium ion insertion in hollow carbon nanowires for battery applications, *Nano Lett.*, 2012, **12**(7), 3783–3787.
44 D. Yang, S. Li, D. Cheng, L. Miao, W. Zhong, X. Yang and Z. Li, Nitrogen, sulfur, and phosphorus codoped hollow carbon microtubes derived from silver willow blossoms as a high-performance anode for sodium-ion batteries, *Energy Fuels*, 2021, **35**(3), 2795–2804.
45 N. Sun, Z. Guan, Y. Liu, Y. Cao, Q. Zhu, H. Liu, Z. Wang, P. Zhang and B. Xu, Extended adsorption–insertion model: a new insight into the sodium storage mechanism of hard carbons, *Adv. Energy Mater.*, 2019, **9**(32), 1901351.
46 S. Qiu, L. Xiao, M. L. Sushko, K. S. Han, Y. Shao, M. Yan, X. Liang, L. Mai, J. Feng, Y. Cao and X. Ai, Manipulating adsorption–insertion mechanisms in nanostructured carbon materials for high-efficiency sodium ion storage, *Adv. Energy Mater.*, 2017, **7**(17), 1700403.
47 S. Guo, Y. Chen, L. Tong, Y. Cao, H. Jiao and X. Qiu, Biomass hard carbon of high initial coulombic efficiency for sodium-ion batteries: Preparation and application, *Electrochim. Acta*, 2022, **410**, 140017.
48 D. Cheng, X. Zhou, H. Hu, Z. Li, J. Chen, L. Miao, X. Ye and H. Zhang, The electrochemical storage mechanism of sodium in carbon materials: A study from soft carbon to hard carbon, *Carbon*, 2021, **182**, 758–769.
49 D. Damodar, S. Ghosh, M. U. Rani, S. K. Martha and A. S. Deshpande, Hard carbon derived from sepals of Palmyra palm fruit calyx as an anode for sodium-ion batteries, *J. Power Sources*, 2019, **438**, 227008.
50 Y. R. Rhim, D. J. Zhang, D. H. Fairbrother, K. A. Wepasnick, K. J. Livi, R. J. Bodnar and D. C. Nagle, Changes in Electrical and Microstructural Properties of Microcrystalline Cellulose as Function of Carbonization Temperature, *Carbon*, 2010, **48**, 1012–1024.
51 M. Xinghua and D. Da, Trash to Treasure: From Harmful Algal Blooms to High-Performance Electrodes for Sodium-Ion Batteries, *Environ. Sci. Technol.*, 2015, **49**(20), 12543–12550.
52 K. Wang, Y. Jin, S. Sun, Y. Huang, J. Peng, J. Luo, Q. Zhang, Y. Qiu, C. Fang and J. Han, Low-cost and high-performance hard carbon anode materials for sodium-ion batteries, *ACS Omega*, 2017, **2**(4), 1687–1695.
53 W. Ma, G. Huang, L. Yu, X. Miao, X. An, J. Zhang, Q. Kong, Q. Wang and W. Yao, Synthesis of multi-cavity mesoporous carbon nanospheres through solvent-induced self-assembly: Anode material for sodium-ion batteries with long-term cycle stability, *J. Colloid Interface Sci.*, 2024, **654**, 1447–1457.
54 K. Tang, L. Fu, R. J. White, L. Yu, M. M. Titirici, M. Antonietti and J. Maier, Hollow carbon nanospheres with superior rate capability for sodium-based batteries, *Adv. Energy Mater.*, 2012, **2**(7), 873–877.
55 D. Alvira, D. Antorán and J. J. Manyà, Assembly and electrochemical testing of renewable carbon-based anodes in SIBs: A practical guide, *J. Energy Chem.*, 2022, **75**, 457–477.
56 Z. Xu, F. Xie, J. Wang, H. Au, M. Tebyetekerwa, Z. Guo, S. Yang, Y. S. Hu and M. M. Titirici, All-cellulose-based quasi-solid-state sodium-ion hybrid capacitors enabled by structural hierarchy, *Adv. Funct. Mater.*, 2019, **29**(39), 1903895.
57 F. Niu, J. Yang, N. Wang, D. Zhang, W. Fan, J. Yang and Y. Qian, $MoSe_2$-covered N, P-doped carbon nanosheets as a long-life and high-rate anode material for sodium-ion batteries, *Adv. Funct. Mater.*, 2017, **27**(23), 1700522.

© 2025 The Author(s). Published by the Royal Society of Chemistry